STAR Technical Note: Transverse Spin-Dependent Azimuthal Correlations of Charged Pion Pairs Measured in p$^{\uparrow}$+p Collisions at $\sqrt{s} = 500$ GeV

Michael Skoby

IU/CEEM

(Dated: October 5, 2017)

ABSTRACT

The transversity distribution, which describes transversely polarized quarks in a transversely polarized nucleon, is a fundamental component of the current picture of the spin structure of the nucleon, and is only loosely constrained by existing semi-inclusive deep inelastic scattering data. The di-hadron interference fragmentation function, which describes the fragmentation of transversely polarized quarks, is expected to give rise to spin-dependent di-hadron correlations in p$^{\uparrow}$+p collisions. The charge-ordered pion pair asymmetry measurement from $\sqrt{s} = 500$ GeV p$^{\uparrow}$+p collisions at STAR is reported as a function of pion pair transverse momentum, invariant mass and pseudorapidity.

TABLE OF CONTENTS

1. INTRODUCTION

Transversity, $h_1^q(x)$, describes transversely polarized quarks, q, with fractional momentum, x, in a transversely polarized nucleon [1]. Transversity has previously been studied in polarized $p+p$ collisions at $\sqrt{s_{NN}} = 200$ GeV [2] and semi-inclusive deep inelastic scattering(SIDIS) measurements [3]- [7]. Azimuthal di-hadron correlation asymmetries are proportional to the product of transversity and the interference fragmentation function(IFF), and allow for point-to-point extraction of transversity in SIDIS. The IFF is independent of the intrinsic transverse momentum from the hadronization process [8]- [9], allowing for the universality of the IFF between $p+p$ and SIDIS to be tested. However, high precision data is lacking at relatively high x, which can be seen in ref. [10]. The high-precision $\pi^+\pi^-$ correlation asymmetry in polarized $p+p$ collisions at $\sqrt{s_{NN}} = 500$ GeV, presented in this analysis, probes a new range of x compared to recent measurements in polarized $p+p$ collisions at $\sqrt{s_{NN}} = 200$ GeV. This measurement will also help constrain the transversity due to the d-quark, which is charge-suppressed in SIDIS.

2. DATA

Dataset:

- Run 2011 transverse $p^{\uparrow} + p$ at $\sqrt{s} = 500$ GeV
- Integrated luminosity $\approx 25\ pb^{-1}$
- Average beam polarization $\approx 53\%$
- $|z\text{-vertex}| < 90$ cm

Track Selection:

- Particle pseudo-rapidity: -1 $\leq \eta \leq 1$
- $p > 2$ GeV/c
- Number of fit points > 15
- Number of fit points/possible > 0.51
- Number of dE/dx hits > 20
- dca < 1 cm
- -1 $\leq n\sigma_{\pi} \leq 2$

Pair Selection:

- $p_T^{\pi^+\pi^-} \geq 3.75$ GeV/c
- Pion separation $\sqrt{(\Delta\eta)^2 + (\Delta\phi)^2} \leq 0.7$

3. KINEMATICS

3.1 Pion Pairs

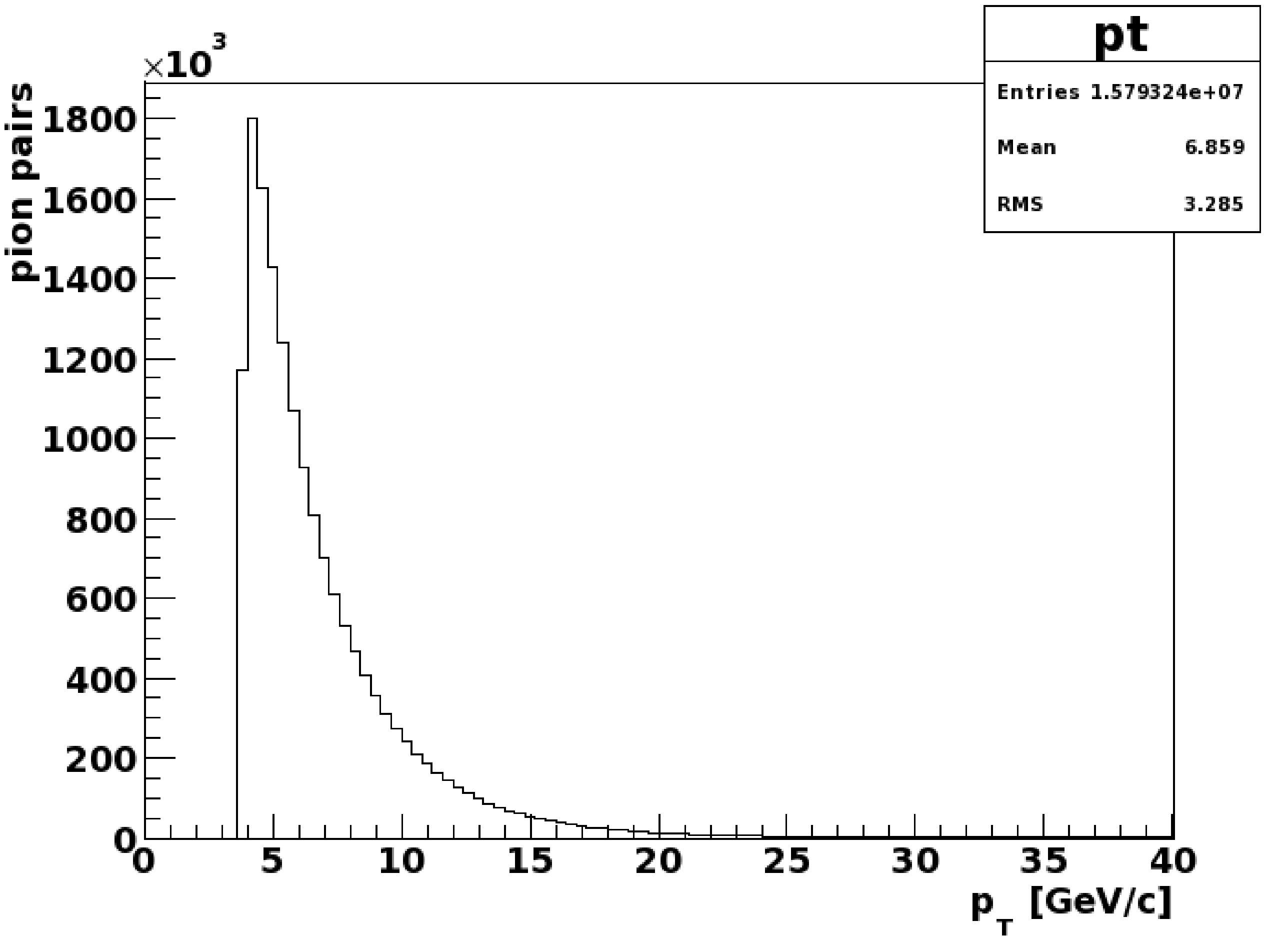

Fig. 3.1. Distribution of p_T for pion pairs.

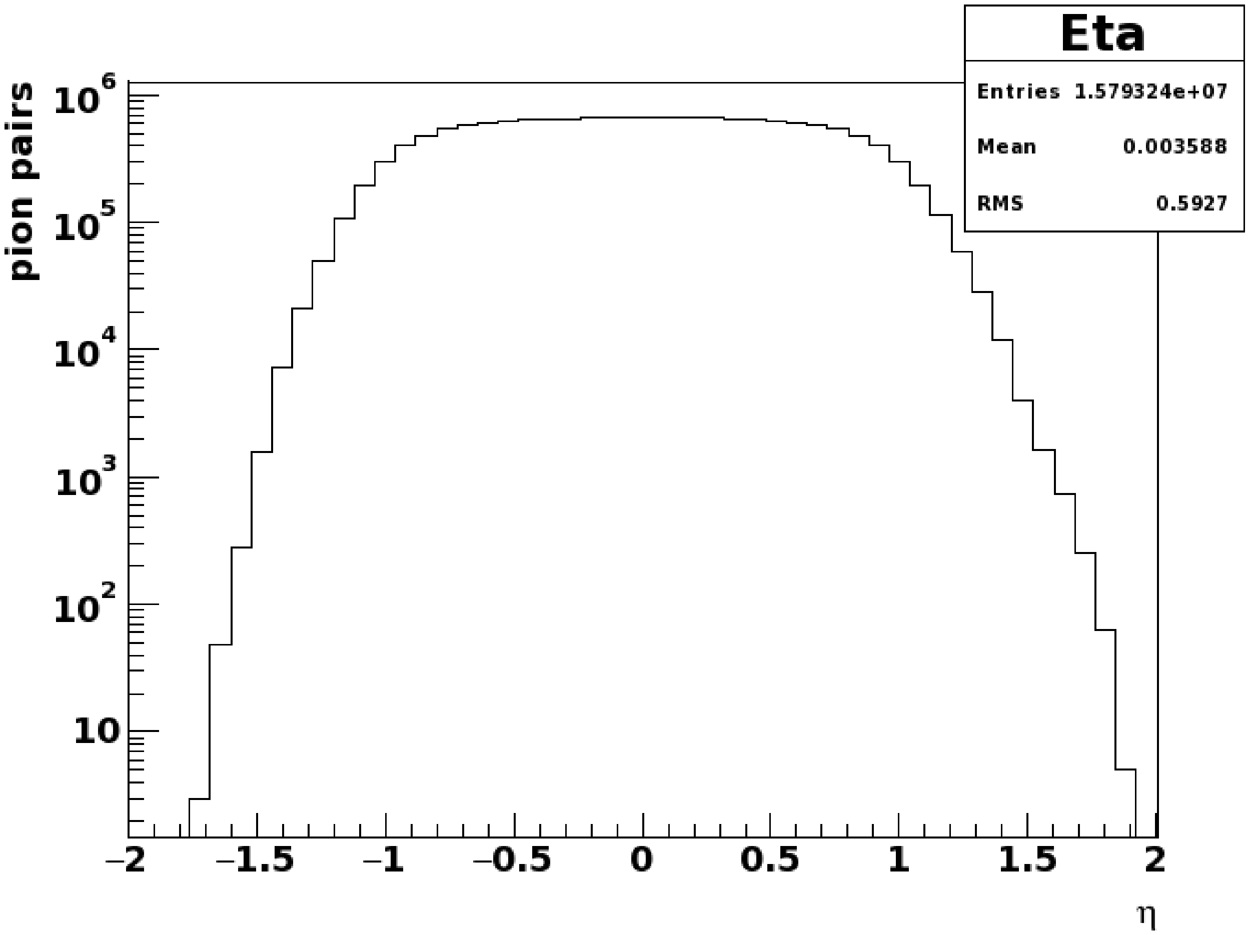

Fig. 3.2. Distribution of η for pion pairs.

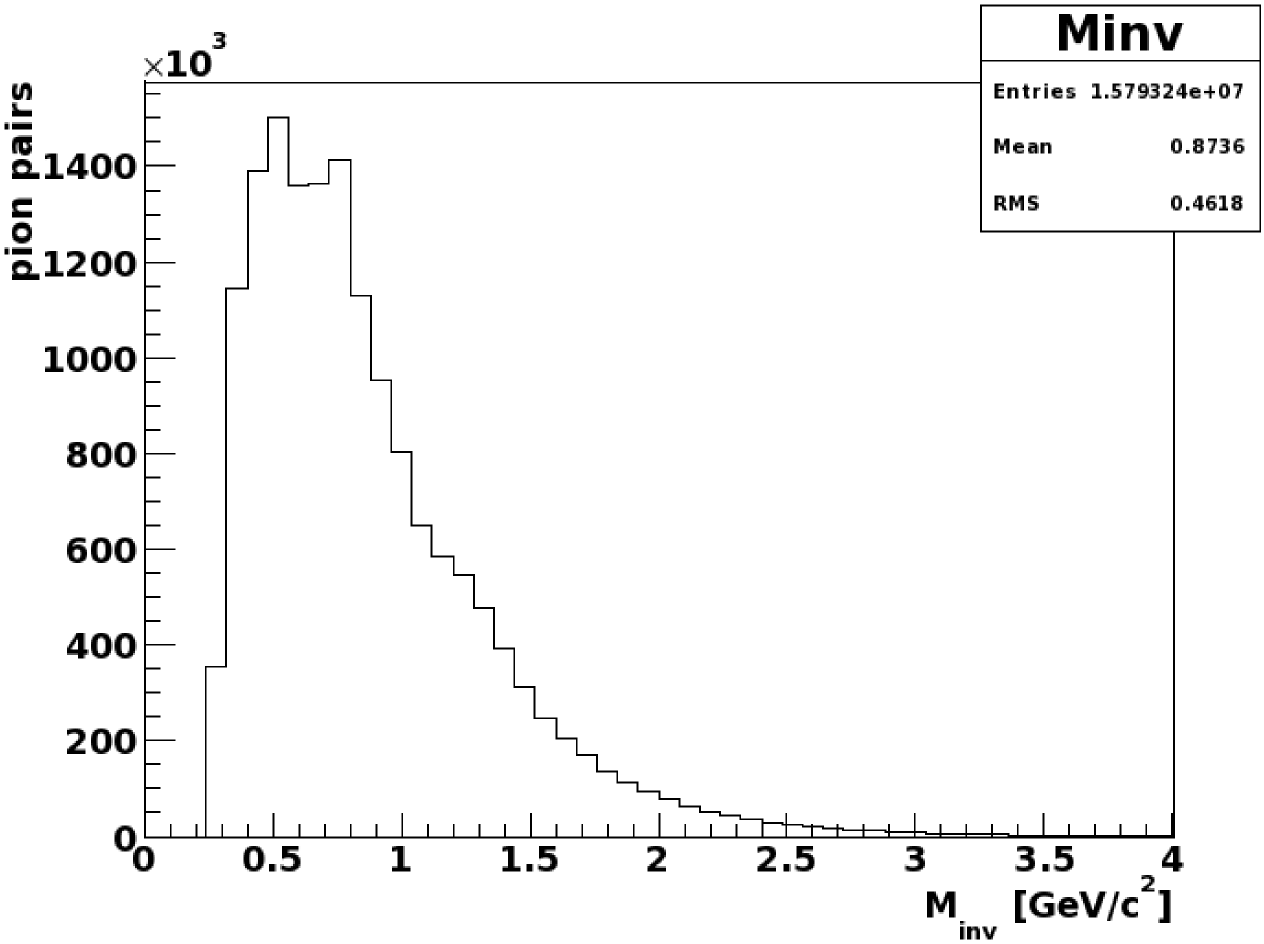

Fig. 3.3. Distribution of M_{inv} for pion pairs.

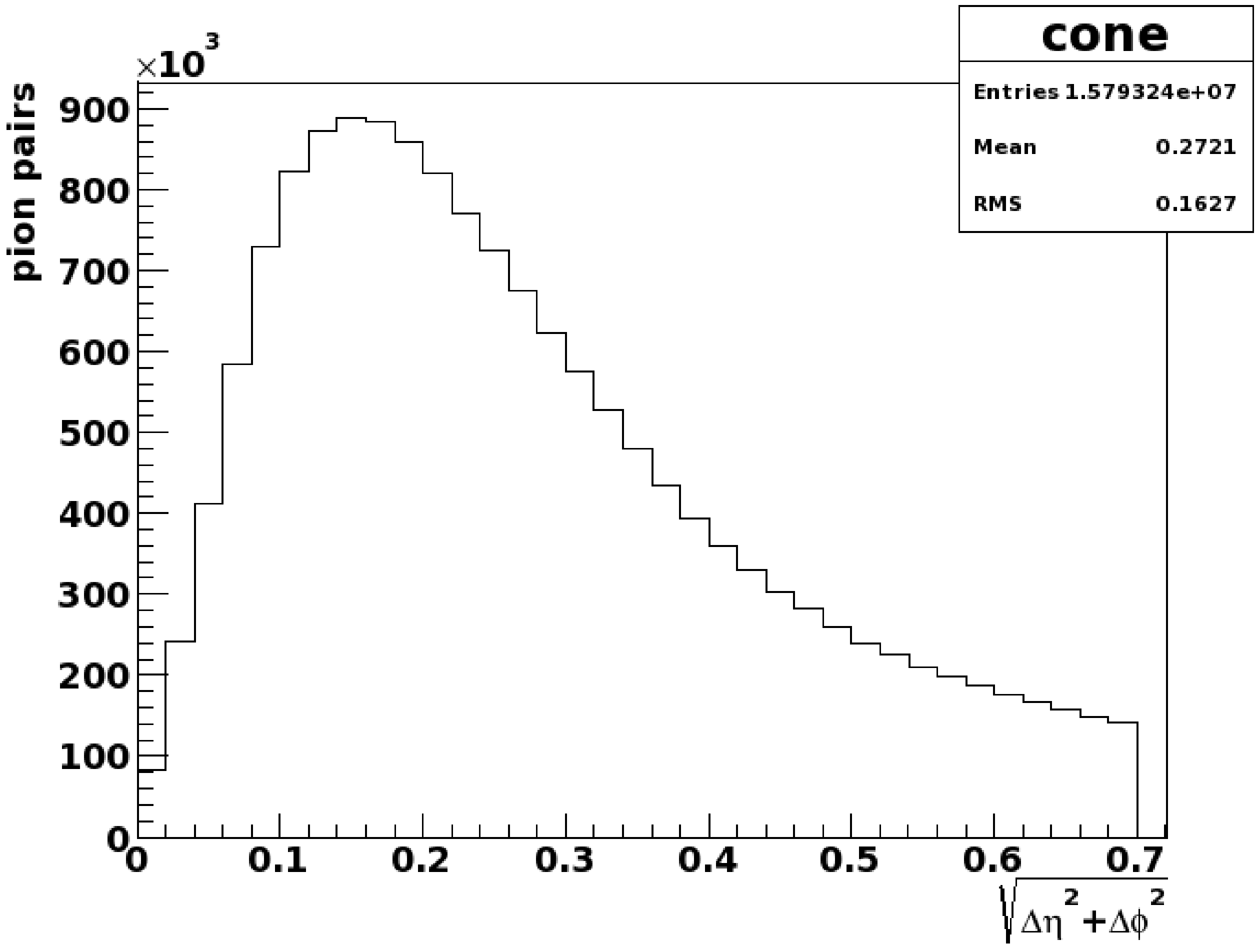

Fig. 3.4. Distribution of the separation between pions within a pair, $\sqrt{\Delta\eta^2 + \Delta\phi^2}$. Only pairs with a separation < 0.7 were used in the analysis.

4. ANALYSIS

4.1 Code Location and Instructions

1. cvs co offline/paper/psn0661/
2. cd offline/paper/psn0661/
3. star-submit run11pp500.xml, which will process run11pp500.C
4. To run over the output in (1) submit iff500_code/Analysis.xml, which will process submitScript.C and StRoot/Iff2012/Iff2012.cc.
5. *hadd* the output from (2) into one file.
6. From iff500_code/ and using the file in (3), run asymmetryVsPt.C, asymmetryVsMinv.C, asymmetryVsMinv_p-Ordered.C, and asymmetryVsEta.C to get the multi-panel result plots

4.2 Particle Identification

Particles are identified by measuring their average specific ionization energy loss $\langle dE/dx \rangle$ as they traverse the TPC and comparing it with the associated theoretical expectation for each particle species.

The theoretical energy loss expectation for a charged particle traveling through a medium is based on the Bethe-Bloch equation shown in Eq. (4.1) [?], where N_0 is Avogadro's number, m_e is the electron mass, Z is the atomic number of the medium, ρ is the density of the medium, z is the charge of the particle traversing the medium, I is the ionization potential of the medium, δ is the medium density correction, and β and γ are the familiar relativistic factors.

$$-\frac{dE}{dx} = 4\pi N_0 r_e^2 m_e c^2 \frac{Z}{A} \rho \frac{1}{\beta^2} z^2 \left[\ln\left(\frac{2m_e c^2}{I} \beta^2 \gamma^2 \right) - \beta^2 - \frac{\delta}{2} \right] \tag{4.1}$$

A parameterization for each particle species is used for comparison with the data as shown in Eq. (4.2), where A is a parameter extracted from the data [53].

$$\left\langle \frac{dE}{dx} \right\rangle = A\left(1 + \frac{m^2}{p^2}\right) \tag{4.2}$$

In comparing the measured energy loss with the theoretical expected energy loss the z variable is introduced in Eq. (4.3) for each particle species [54].

$$z = \ln\left(\frac{dE/dx_{measured}}{dE/dx_{parameterized}}\right) \tag{4.3}$$

The z variable is calculated for each species on all measured tracks. Cuts on the number of standard deviations (nσ) from the peak are also used to identify particles.

Figures 4.1- 4.3 show $n\sigma(\pi)$ vs $n\sigma(K, p, e)$ for various p and η bins. A 3rd order polynomial is fit to the distributions to get the separation between the pion-kaon, pion-proton, and pion-electron peaks in the $n\sigma(\pi)$ distribution. Figure refpid4 shows these peak separations for kaons and protons. Each segment is a momentum bin, with momentum decreasing with increasing index. Within each segment, η increases with increasing index. The separation between kaons and protons is small for middle momentum bin ($2.5 < p < 3$ GeV), therefore, a single Gaussian is used to account for both species. For the middle η bins, the separation between pions and protons in the smallest momentum bin (indexes 22-24) is too small to get distinguishable Gaussians, thus, a cut of $p < 2$ GeV was applied. Figure 4.5 shows the Gaussian fits for each particle species to the $n\sigma(\pi)$ distributions. These fits are used to estimate the pion purity for $p - eta$ bin and are shown in the upper left corner of each plot. These purities are used to estimate the probability that both particles in a pair are pions, which is shown in figure 4.6 for the kinematic variables for which the asymmetry is measured. The overall pion pair purity is about 85%, and is used to get the identified pion systematic uncertainty (.15*asymmetry).

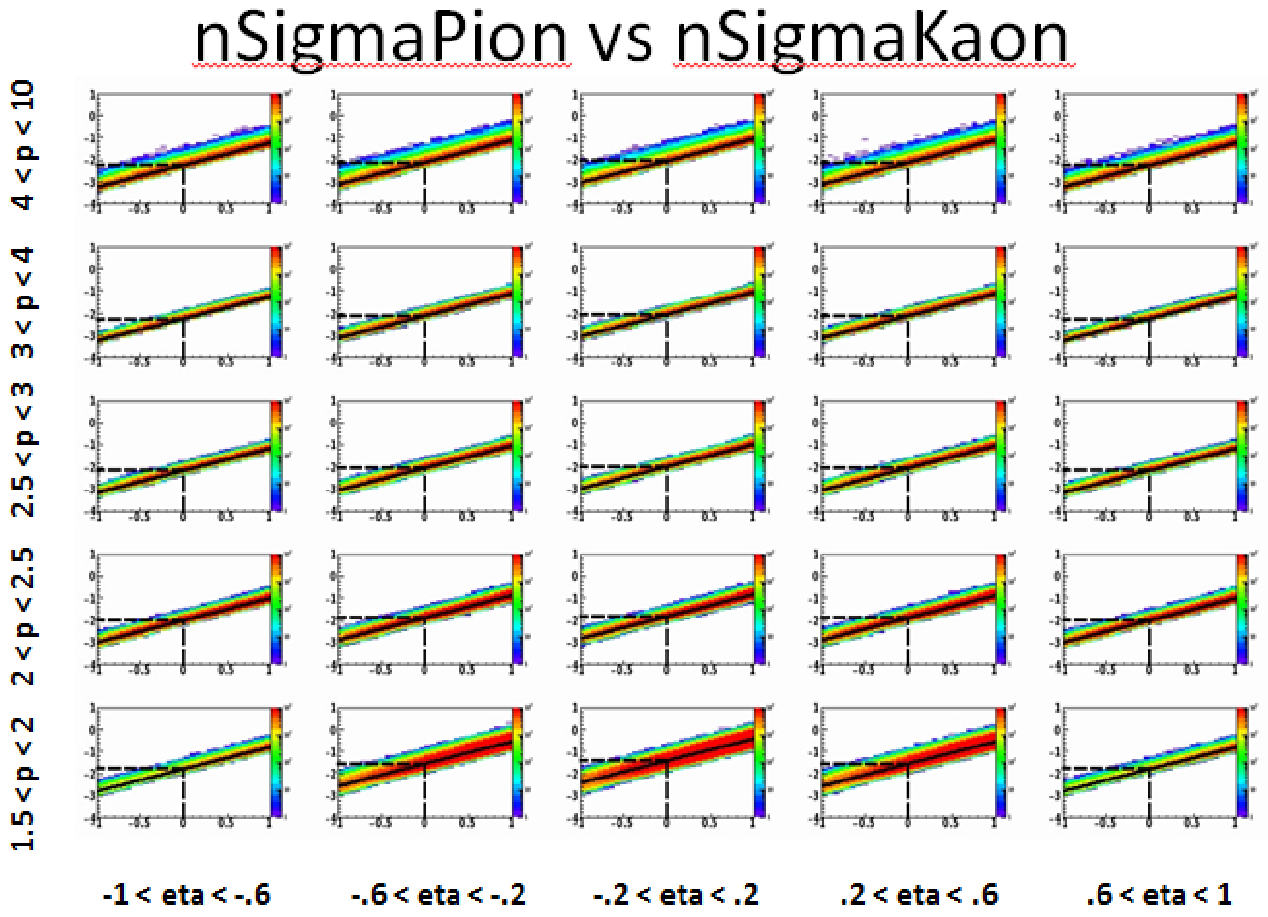

Fig. 4.1. $n\sigma(\pi) vs n\sigma(K)$ distributions for various particle p and η bins.

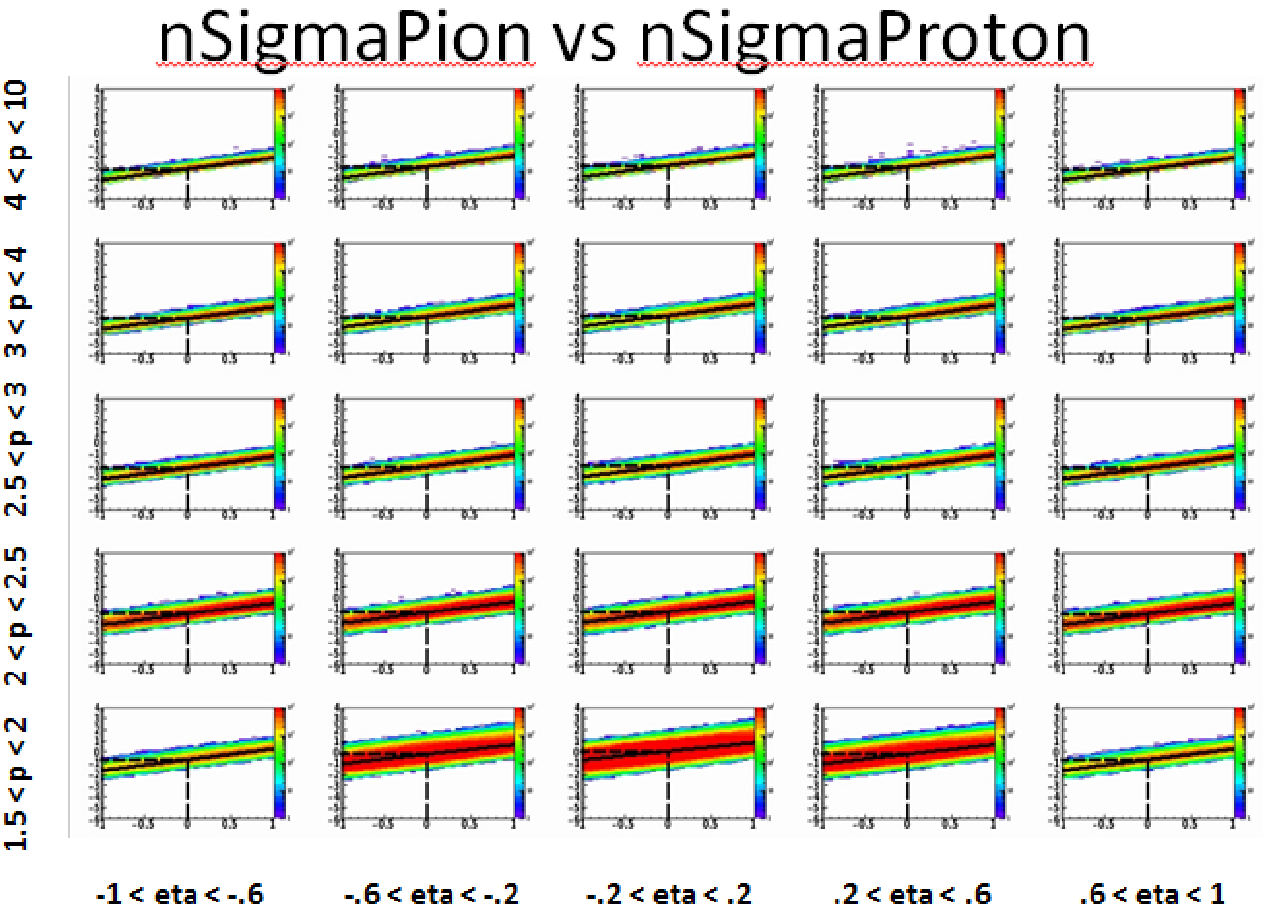

Fig. 4.2. $n\sigma(\pi) vs n\sigma(p)$ distributions for various particle p and η bins.

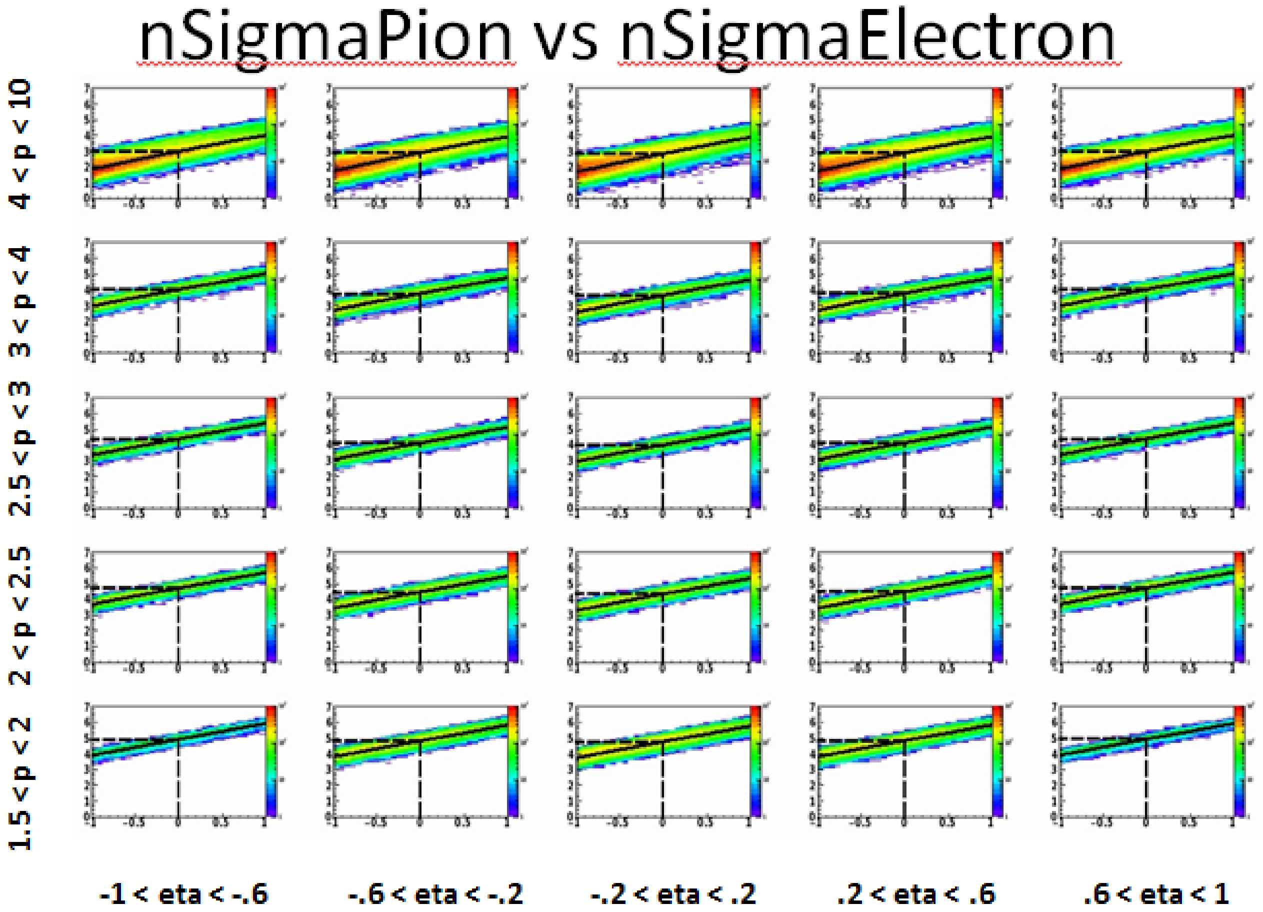

Fig. 4.3. $n\sigma(\pi) vs n\sigma(e)$ distributions for various particle p and η bins.

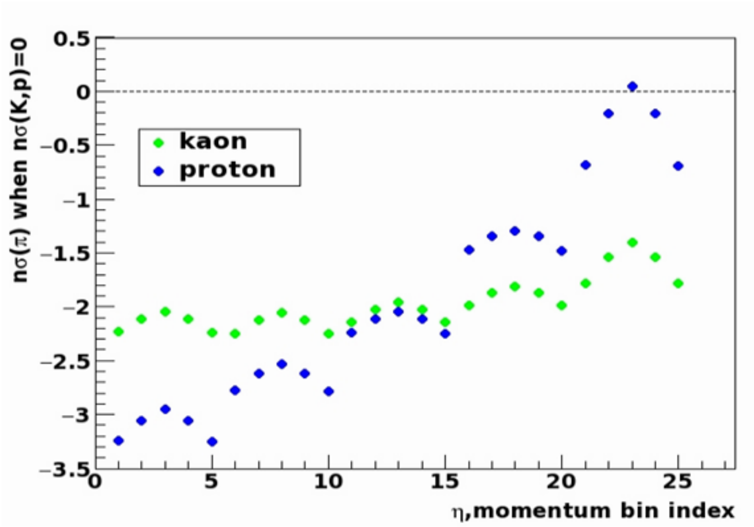

Fig. 4.4. $n\sigma(\pi)$ when $n\sigma(K,p) = 0$ for various p and η bins. Each segment is a p bin, with p decreasing with increasing index. Within each segment, η increases with increasing index.

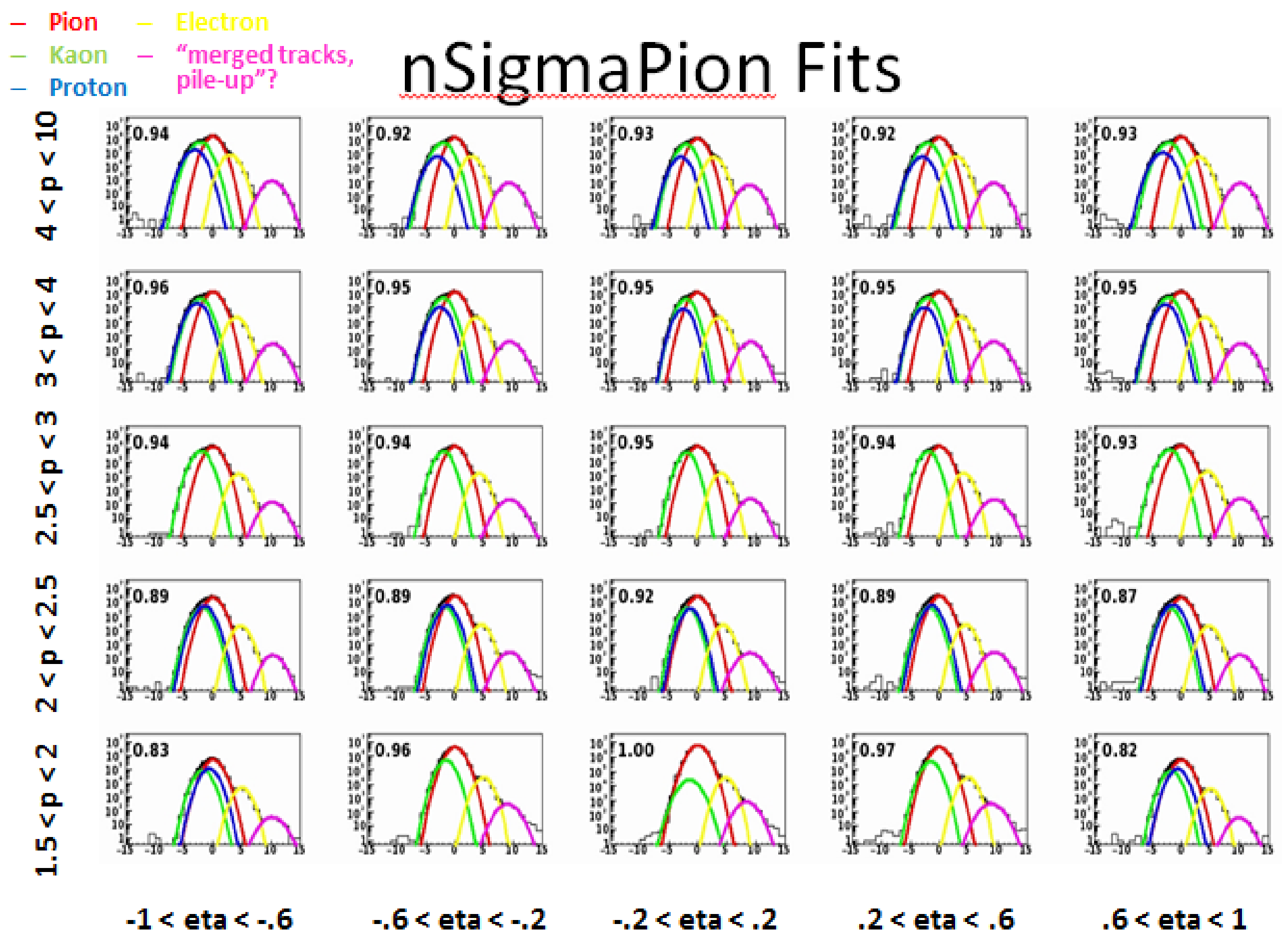

Fig. 4.5. $n\sigma(\pi)$ distributions for various particle p and η bins with particle species fits. The pion purity is shown in the upper left corner of each plot.

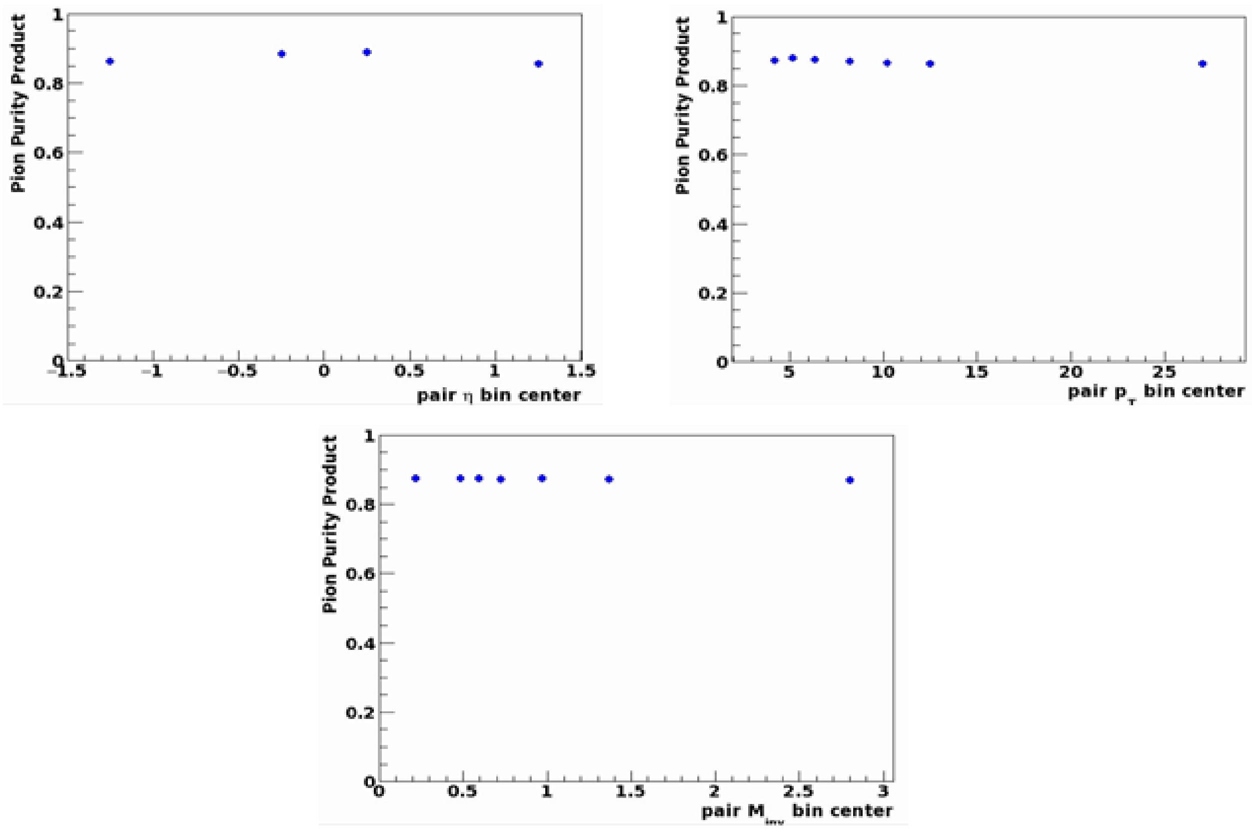

Fig. 4.6. The pion purity product is the probability that both particles in a pair are pions, shown here as a function of the kinematic bins for which the asymmetry was measured.

4.3 Asymmetry Calculation

The azimuthal angles in the scattering system used to calculate the $\pi^+\pi^-$ correlation asymmetry are shown in Fig. 4.7, where the scattering plane is defined by the polarized beam direction, $\overrightarrow{P}_B$, and the direction of the total momentum of the pion pair, $\overrightarrow{P}_C$. The two-hadron plane is defined by the momentum vectors from each pion in the pair, where the pions are chosen to be in close proximity to each other in $\eta - \phi$ space with $\sqrt{(\Delta\eta)^2 + (\Delta\phi)^2} \leq 0.7$. The angle between the scattering plane and the polarization of the incident beam, $\overrightarrow{S}_B$, is ϕ_S. The angle between the scattering plane and the two-hadron plane is ϕ_R, which is used to define $\phi_{RS} = \phi_R - \phi_S$.

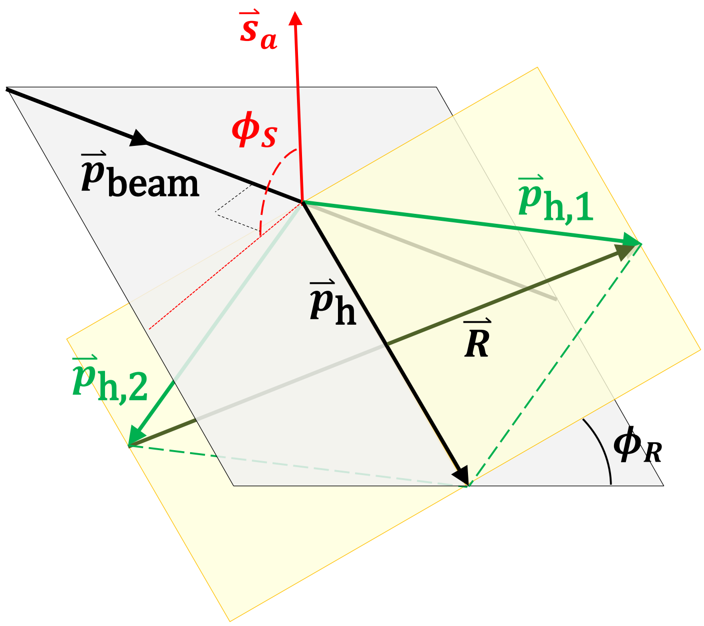

Fig. 4.7. Azimuthal angle diagram.

The $\pi^+\pi^-$ correlation asymmetry observable is defined in ref. [12], but an alternative form, independent of the relative luminosity, is used in this analysis [13]:

$$A_{UT}(\phi_{RS}) = \frac{1}{P}.\frac{\sqrt{N\uparrow(\phi_{RS})N\downarrow(\phi_{RS}+\pi)} - \sqrt{N\downarrow(\phi_{RS})N\uparrow(\phi_{RS}+\pi)}}{\sqrt{N\uparrow(\phi_{RS})N\downarrow(\phi_{RS}+\pi)} + \sqrt{N\downarrow(\phi_{RS})N\uparrow(\phi_{RS}+\pi)}}. \tag{4.4}$$

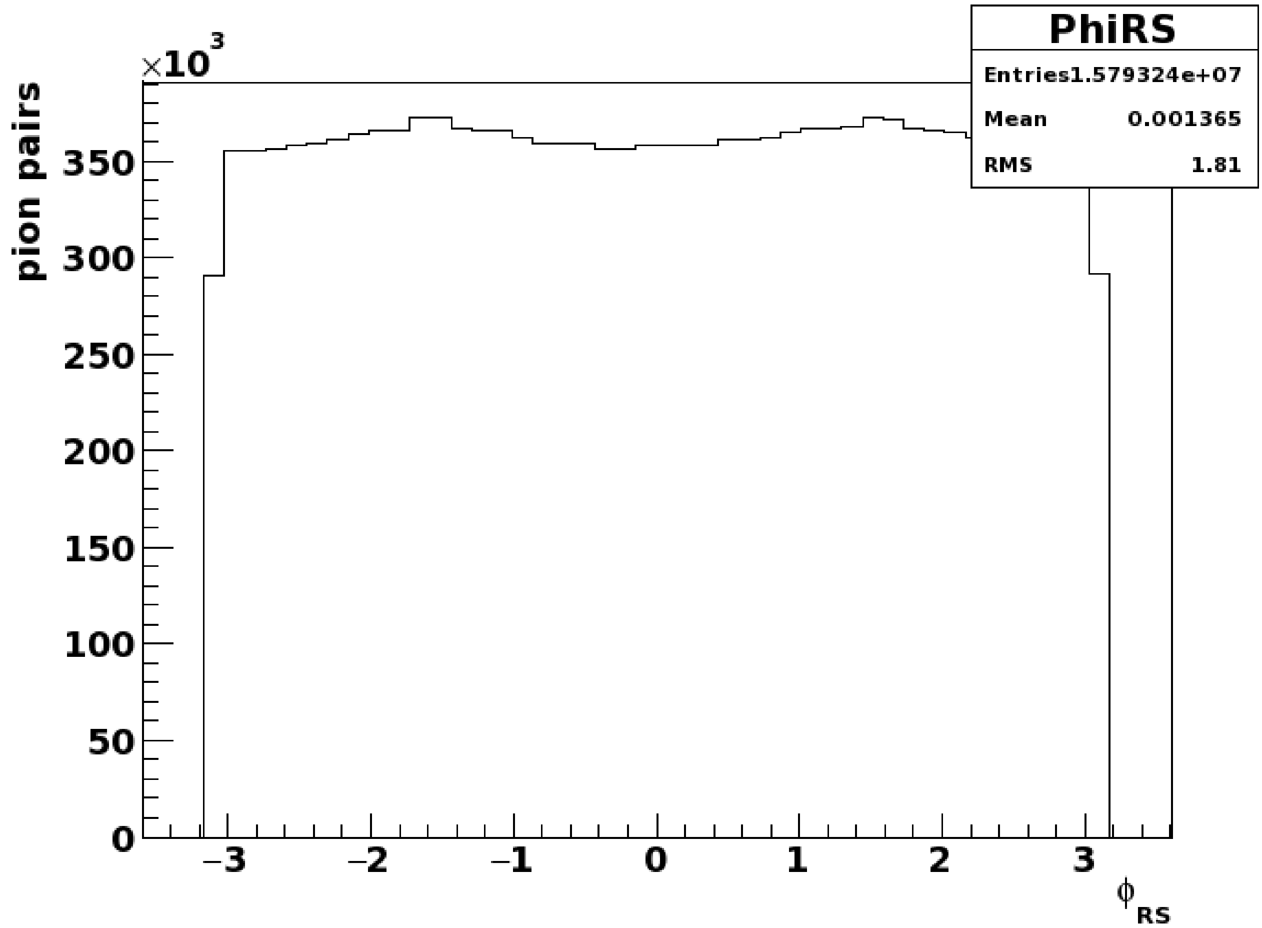

Fig. 4.8. Distribution of ϕ_{RS} for pion pairs.

In eq. (1), P is the beam polarization and $N\uparrow(\downarrow)$ is the number of pion pairs when the polarized beam is polarized up(down). A_{UT} is calculated for 8 ϕ_{RS} bins of equal width, which is then fitted with a single-parameter function, $A_{UT}sin(\phi_{RS})$, to extract the asymmetry. This procedure is carried out as a function of the η of the pion pair, $\eta^{\pi^+\pi^-}$, where $\eta^{\pi^+\pi^-} > (<)\ 0$ is forward(backward) with respect to the polarized beam direction. A_{UT} is also measured for several invariant mass bins, $M_{\pi^+\pi^-}$, and $p_T^{\pi^+\pi^-}$.

4.4 Trigger Bias

A potential bias in the data may be due to event triggering. Since quark jets are more collimated than gluon jets, triggered events are biased towards pions that fragment from quark jets. Due to the chiral-odd nature of gluons, there should be no contribution to the asymmetry from pion pairs that come from gluons. Therefore, the asymmetry measured from data could potentially be enhanced. This trigger bias effect is estimated using particles produced in simulation from Pythia and reconstructing them through GEANT. The source parton for each pion pair was chosen by matching the pion pair to the outgoing parton closest in (η,ϕ)-space and requiring the pair-parton separation to be less than 0.5. For each partonic p_T bin the ratio of matched quarks/partons in a biased sample (GEANT) to matched quarks/partons in an unbiased sample (Pythia) is used to estimate the trigger bias effect:

$$R = \frac{quarks/partons(GEANT)}{quarks/partons(Pythia)}. \tag{4.5}$$

The quark and gluon reconstruction efficiencies are defined in 4.6 and plotted in Fig. 4.10.

$$\epsilon_q = \frac{quarks(GEANT)}{quarks(Pythia)}, \epsilon_g = \frac{gluons(GEANT)}{gluons(Pythia)} \tag{4.6}$$

Using the efficiencies in 4.6, equation 4.5 can be rewritten as:

$$R = \frac{\epsilon_q(q+g)}{\epsilon_q q + \epsilon_g g},, \tag{4.7}$$

where q and g are the Pythia quarks and gluons, respectively. The form in 4.7 was chosen because the uncertainty on the efficiencies is known and the uncertainty on the Pythia quark and gluon counts is smalled compared to the efficiency uncertainty. For each trigger, R is shown in Fig. 4.11 and the event-weighted average over triggers is shown in Fig. 4.12.

The fraction of pairs in each pair-p_T bin that come from a given partonic-p_T bin are shown in Fig. 4.13. Since R is calculated by partonic p_T bin, these fractions,f, are used to estimate the trigger bias effect on each pair p_T bin via equation 4.8.

$$R_{pair} = \sum_{i=1}^{10} f_i R_i, \tag{4.8}$$

where i is the ith partonic p_T bin. The trigger decision is based on the energy deposit in a defined segment in one of the calorimeters. We expect therefore that the trigger bias effect will be strongest for low p_T parent jets, since at high jet p_T the impact of the shape difference between quark or gluon initiated jets will negligible for the trigger decision. For this reason we investigated the trigger bias as a function of the transverse momentum of the hadron pair. Within our statistical uncertainties, we do not observe a significant trigger bias. Instead, the statistical uncertainty with which one can determine the ratio of the fractions of quark initiated jets in the triggered over the non-triggered sample was assigned as a systematic uncertainty, being $\sim$20% at low p_T and $\sim$5% at high p_T. Note that the trigger bias does not affect the statistical significance of the measurement since the scaling applies to the asymmetry and its uncertainty equally.

Finally, the pion pair purity previously mentioned was used to estimate the asymmetric asymmetry dilution due to $\pi - K$ and $\pi - p$ pairs to be about 15% and is shown as rectangles above(below) positive(negative) data points.

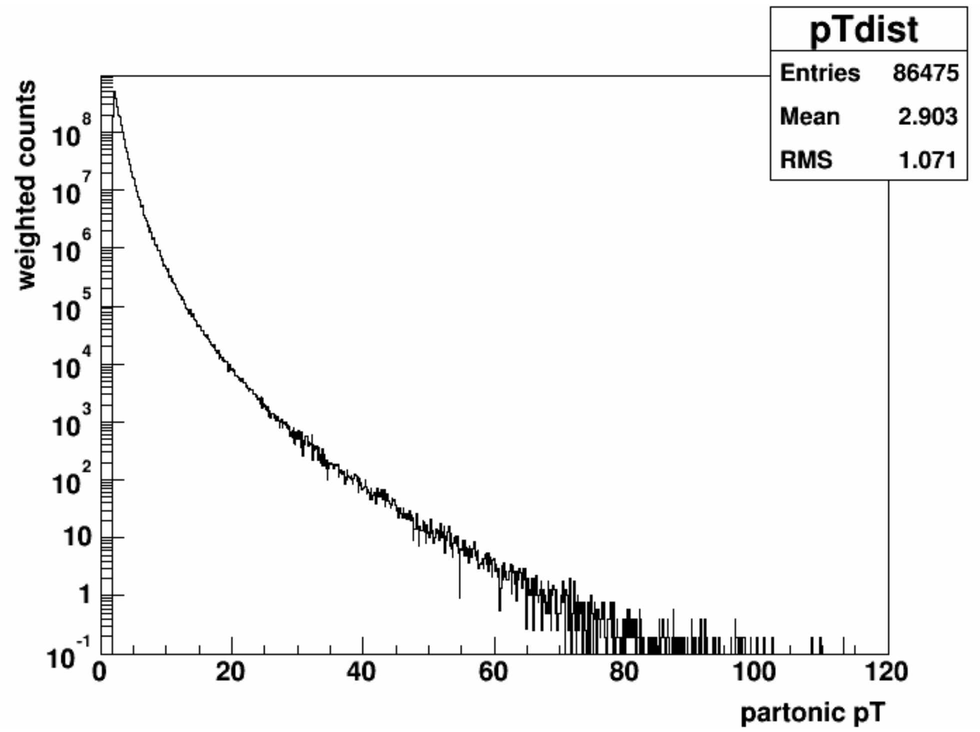

Fig. 4.9. Weighted partonic p_T distribution of partons from simulation.

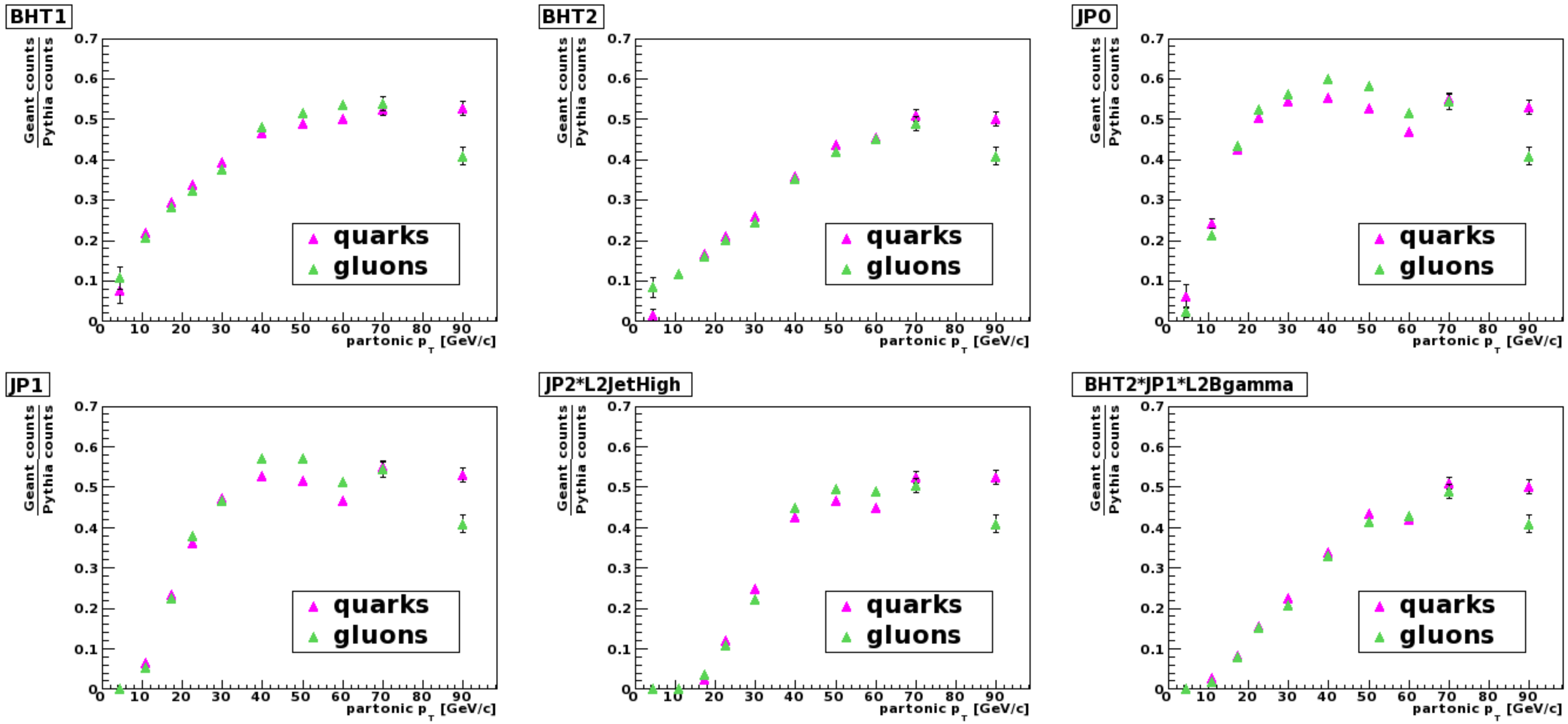

Fig. 4.10. Quarks and gluons reconstructed in Geant divided by those in the original Pythia sample.

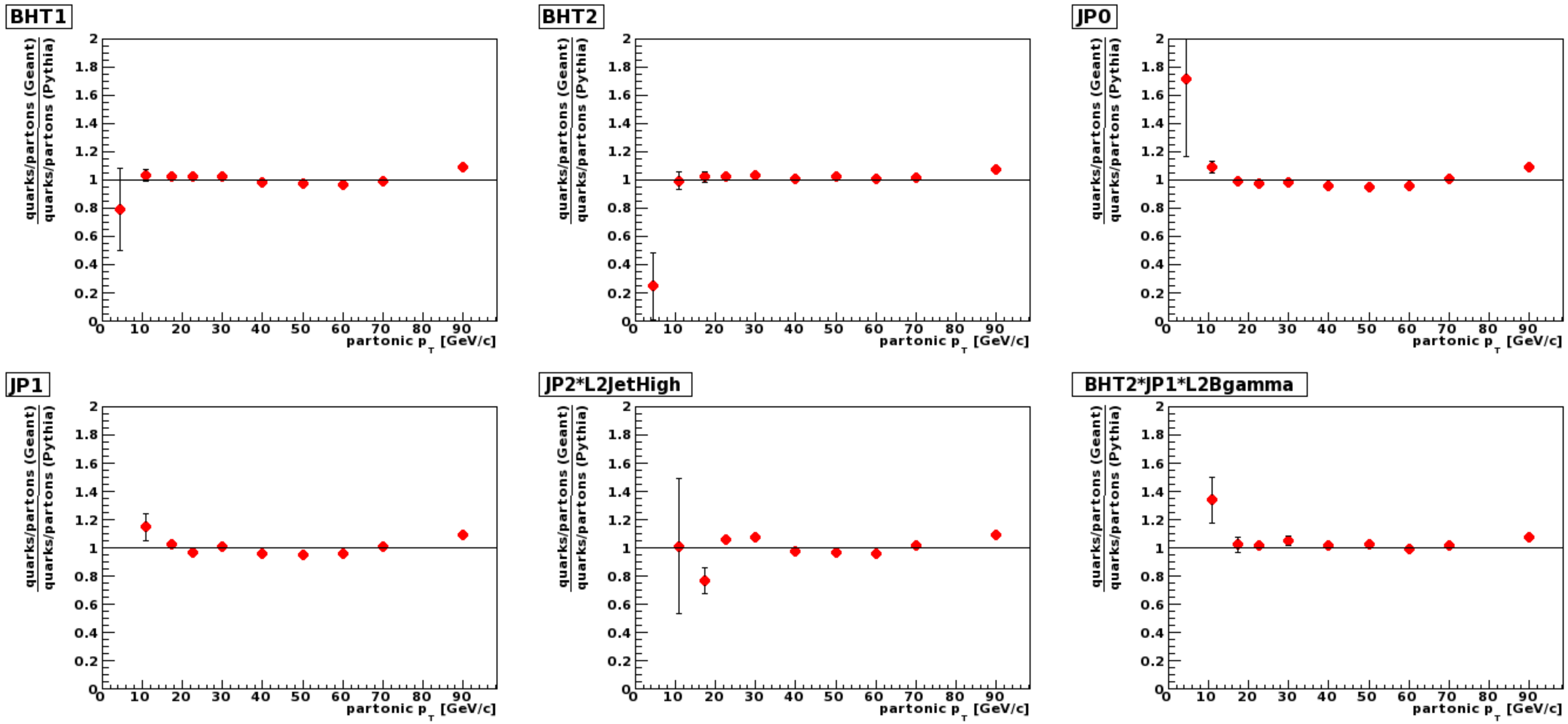

Fig. 4.11. Quark to parton ratio from Geant divided by the ratio from Pythia.

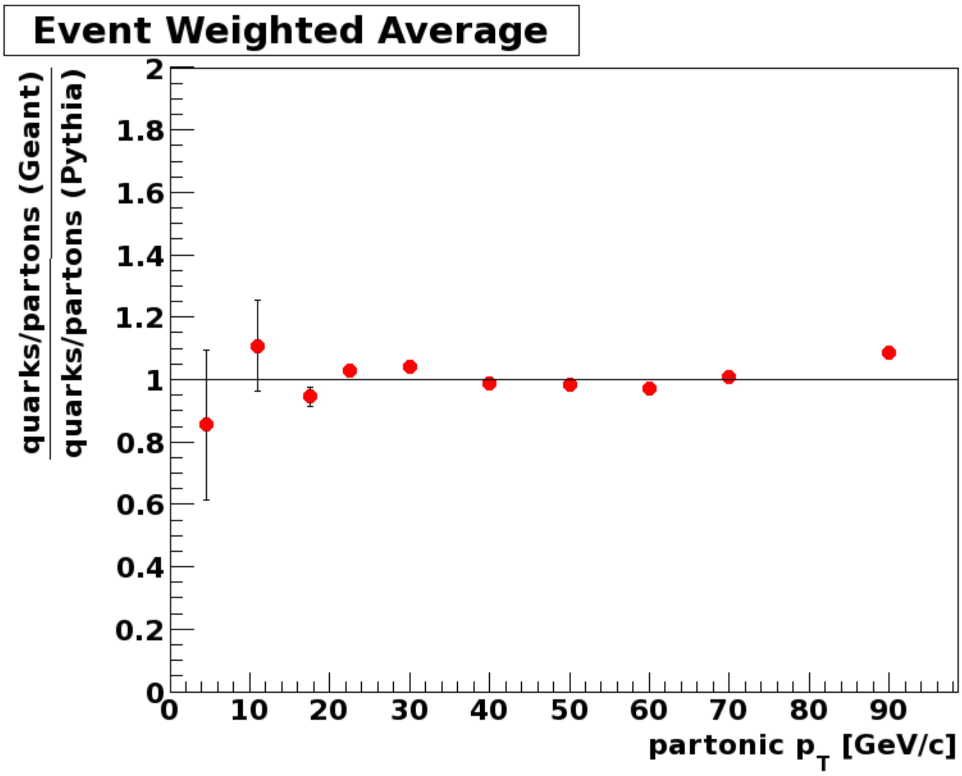

Fig. 4.12. Average quark to parton ratio from Geant divided by the ratio from Pythia weighted by data events over all triggers.

4.5 x, z Estimations

The simulations used to find the trigger bias effect above were also used to estimate the kinematic variables x and z, where x is the fractional momentum of quarks associated with the poin pairs, and z is the fraction of energy of quarks carried by pion pairs. x and z as a function of pion pair pseudorapidity is shown in the bottom panel of Fig. 5.1 in the results section. An example of the x distribution in the partonic bin 55-65 GeV for 4 η bins is shown in Fig. 4.14.

PARTONIC p_T [GeV/c]	PAIR p_T [GeV/c]						
	4	5	6	8	10	12	18
4.5	0.653	0.393	0.367	0	0	0	0
11	0.281	0.483	0.473	0.582	0.498	0.448	0.060
17.5	0.044	0.078	0.095	0.238	0.267	0.232	0.155
22.5	0.014	0.028	0.038	0.102	0.132	0.153	0.288
30	0.006	0.014	0.021	0.058	0.075	0.123	0.305
40	0.001	0.003	0.005	0.015	0.019	0.030	0.132
50	0	0.001	0.001	0.003	0.006	0.010	0.038
60	0	0	0	0.001	0.002	0.003	0.014
70	0	0	0	0	0	0.001	0.005
75+	0	0	0	0	0	0	0.003

Fig. 4.13. The fraction of pairs in each pair-p_T bin that come from a given partonic-p_T bin.

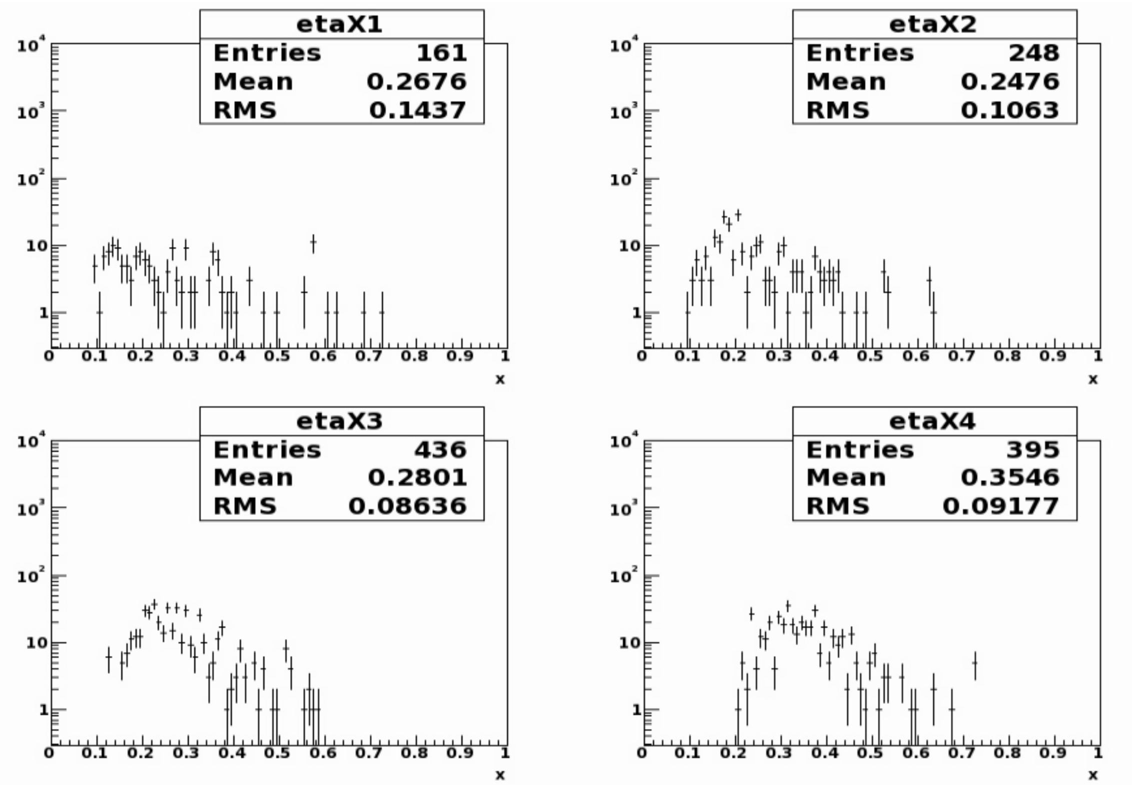

Fig. 4.14. An example of an x distribution in partonic p_T bin 55-65 GeV.

4.6 Spin Transfer Factor

The Mandelstam variables shown below are used to find the spin transfer factor.

$$\hat{s} = (p_1 + p_2)^2 = (p_3 + p_4)^2 \tag{4.9}$$

$$\hat{t} = (p_1 - p_3)^2 = (p_2 - p_4)^2 \tag{4.10}$$

$$\hat{u} = (p_1 - p_4)^2 = (p_2 - p_3)^2 \tag{4.11}$$

, where p_1 is the incoming polarized parton, p_2 is the incoming unpolarized parton, and p_3 and p_4 are the scattered partons. The spin transfer factor, $\hat{d}_{NN}$, is show below for various reactions indicated in braces.

$$\frac{-2\hat{s}\hat{u}(1-\frac{\hat{t}}{3\hat{u}})}{\hat{s}^2+\hat{u}^2+(\hat{s}^2+\hat{t}^2)\frac{\hat{t}^2}{\hat{u}^2}-2\hat{s}^2\frac{\hat{t}}{3\hat{u}}} \begin{cases} qq \rightarrow qq \\ \bar{q}\bar{q} \rightarrow \bar{q}\bar{q} \end{cases} \tag{4.12}$$

$$\frac{-2\hat{s}\hat{u}(1-\frac{\hat{t}}{3\hat{s}})}{\hat{s}^2+\hat{u}^2+(\hat{u}^2+\hat{t}^2)\frac{\hat{t}^2}{\hat{s}^2}-2\hat{u}^2\frac{\hat{t}}{3\hat{s}}} \begin{cases} q\bar{q} \rightarrow q\bar{q} \\ \bar{q}q \rightarrow \bar{q}q \end{cases} \tag{4.13}$$

$$\frac{-2\hat{s}\hat{u}}{\hat{s}^2+\hat{u}^2} \begin{cases} qq' \rightarrow qq' \\ q\bar{q} \rightarrow q'\bar{q}' \\ \bar{q}q \rightarrow \bar{q}'q' \\ qG \rightarrow qG \\ \bar{q}G \rightarrow \bar{q}G \end{cases} \tag{4.14}$$

5. RESULTS

A_{UT} as a function of $\eta^{\pi^+\pi^-}$ is shown in Fig. 5.1 for the highest $p_T^{\pi^+\pi^-}$. Since valence quarks of the incident proton, described by transversity, have large x, transversity will be manifested in forward pion pairs, resulting in the significant rise of the asymmetry for increasing $\eta^{\pi^+\pi^-}$ in the highest $p_T^{\pi^+\pi^-}$ bin as shown in Fig. 5.1.

A_{UT} as a function of $M_{\pi^+\pi^-}$ for $\eta^{\pi^+\pi^-} > 0$ is shown in Fig. 5.3 for the highest $p_T^{\pi^+\pi^-}$. A significant signal is seen in the highest $p_T^{\pi^+\pi^-}$ bin, with an enhancement near the ρ mass at mid-$M_{\pi^+\pi^-}$. This enhancement is expected from the transverse spin dependent IFF due to the interference of vector meson decays in a relative p-wave interfering with the non-resonant background in a relative s-wave. A_{UT} as a function of $M_{\pi^+\pi^-}$ for $\eta^{\pi^+\pi^-} < 0$ is plotted for all $p_T^{\pi^+\pi^-}$ bins in Fig. 5.5. The observed asymmetry is small, as expected, because transversity is manifested in forward $\eta^{\pi^+\pi^-}$ as described above.

Figure **??** shows the asymmetry as a function of invariant mass for each p_T bin in 5 separate plots.

A_{UT} as a function of $p_T^{\pi^+\pi^-}$ for $\eta^{\pi^+\pi^-} > 0$ is shown in Fig. 5.6 for the highest(magenta) and lowest(black) $M_{\pi^+\pi^-}$. A significant asymmetry is observed at high $p_T^{\pi^+\pi^-}$ in the highest $M_{\pi^+\pi^-}$ bin. All other $M_{\pi^+\pi^-}$ bins are shown in Fig. **??**. A_{UT} is small for $\eta^{\pi^+\pi^-} < 0$ in all $M_{\pi^+\pi^-}$ and $p_T^{\pi^+\pi^-}$ bins.

The largest systematic uncertainty in this analysis comes from the 4.5% scale uncertainty due to the beam polarization. Additionally, the events chosen to be recorded are biased towards pions that fragment from quarks. However, pions that come from gluons should make no contribution to transversity due to the chiral odd nature of gluons [1]. To investigate this bias, a Pythia [14] simulation was used along with GEANT [15] , which models the STAR detector, to estimate the quark/parton

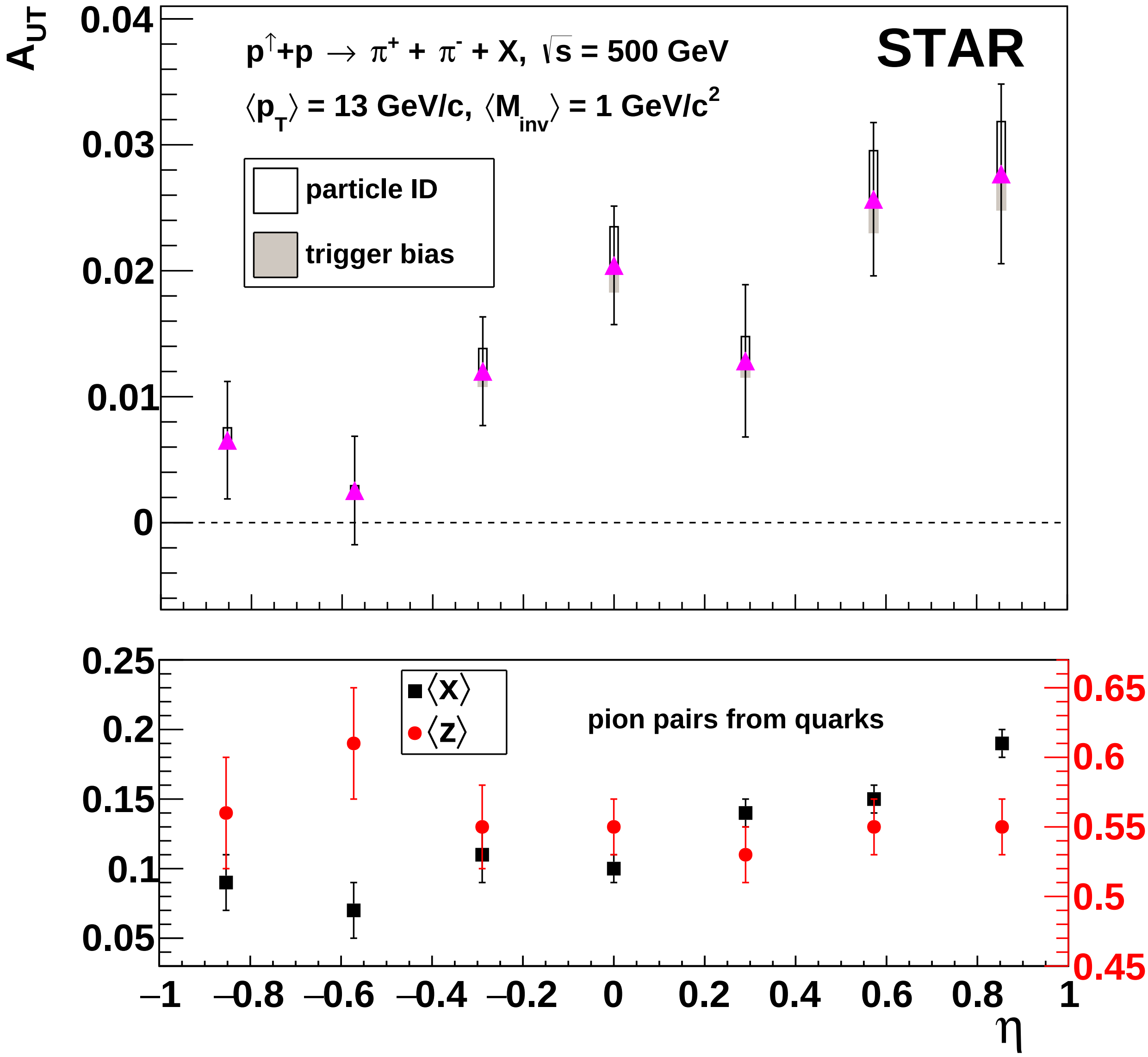

Fig. 5.1. The asymmetry A_{UT} as a function of $\eta^{\pi^+\pi^-}$ for the highest $p_T^{\pi^+\pi^-}$ bin (top panel). (bottom panel) $\langle z \rangle$ and $\langle x \rangle$ as a function of η.

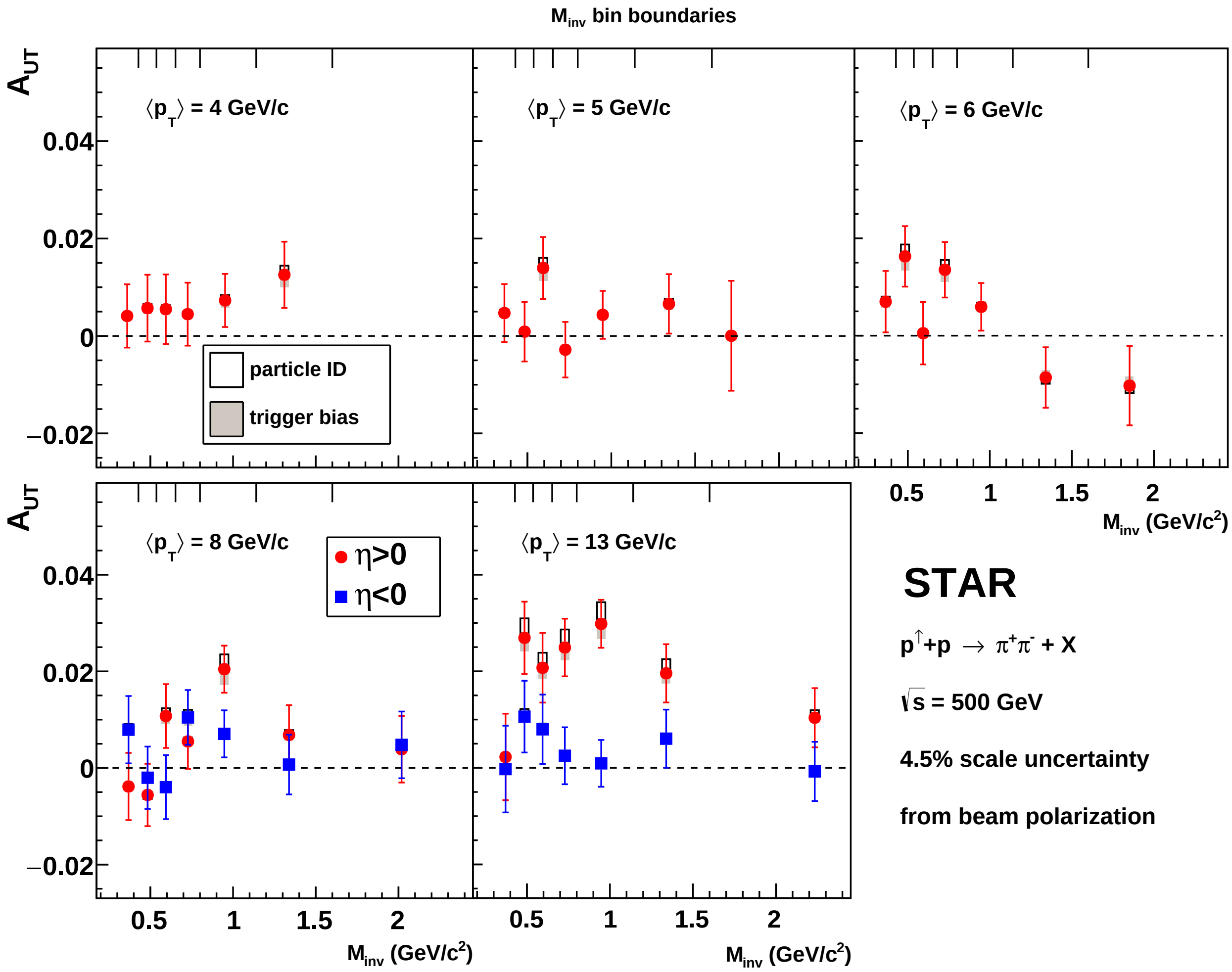

Fig. 5.2. The asymmetry A_{UT} as a function of $M_{\pi^+\pi^-}$ for five $p_T^{\pi^+\pi^-}$ bins and $\eta^{\pi^+\pi^-} > 0$.

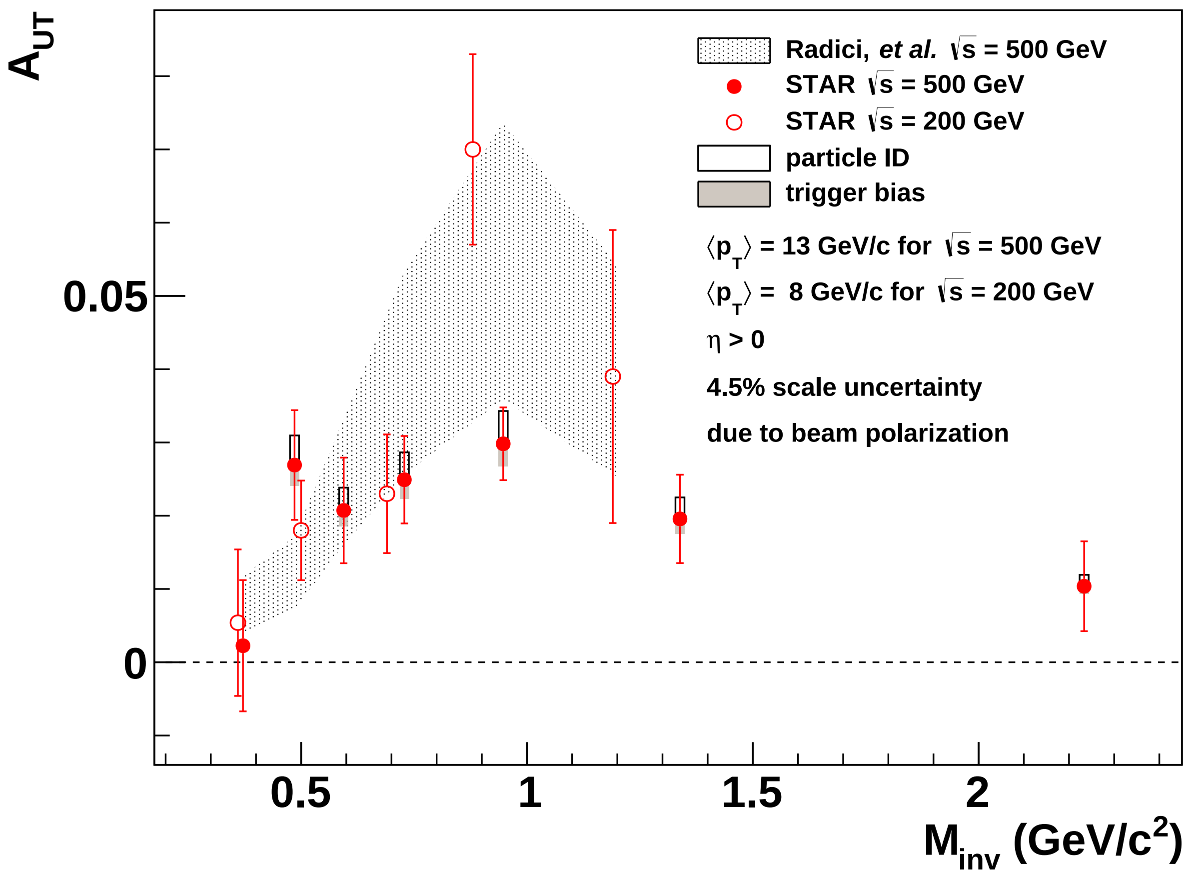

Fig. 5.3. The asymmetry A_{UT} as a function of $M_{\pi^+\pi^-}$ for the largest $p_T^{\pi^+\pi^-}$ bin and $\eta^{\pi^+\pi^-} > 0$. Good agreement is shown between the theory band and data from 200 GeV.

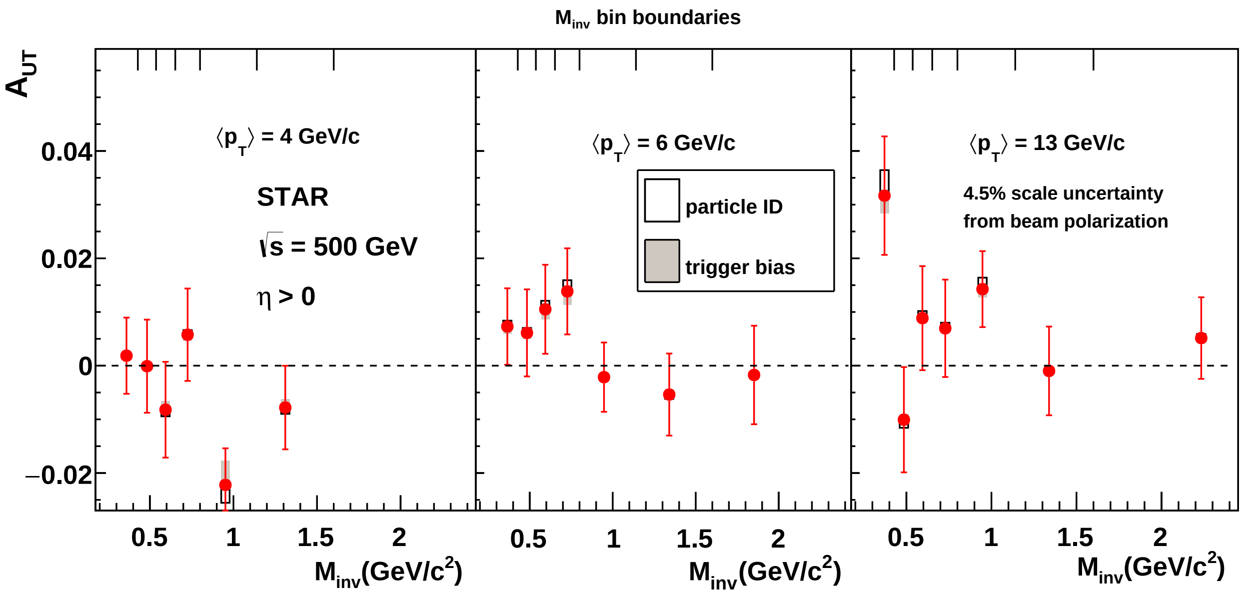

Fig. 5.4. The same-charge, momentum-ordered asymmetry A_{UT} as a function of M_{inv} for the lowest pt_T bin, mid-pt_T bin, and the highest p_T bin. Statistical uncertainties are error bars and the open rectangles are the systematic uncertainties originating from the particle identification. The M_{inv} bin boundaries are shown at the top of the figure.

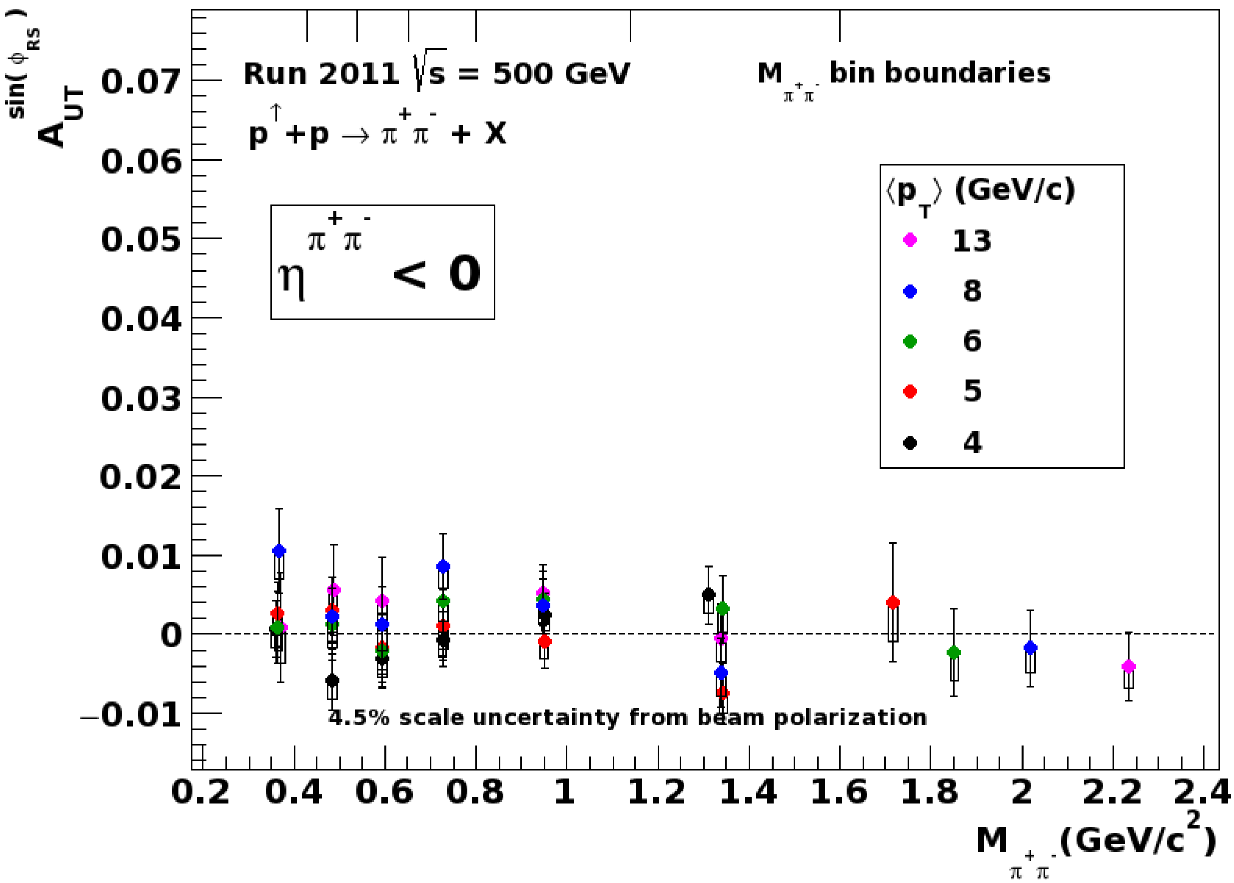

Fig. 5.5. The asymmetry A_{UT} as a function of $M_{\pi^+\pi^-}$ for all $p_T^{\pi^+\pi^-}$ bins and $\eta^{\pi^+\pi^-} < 0$.

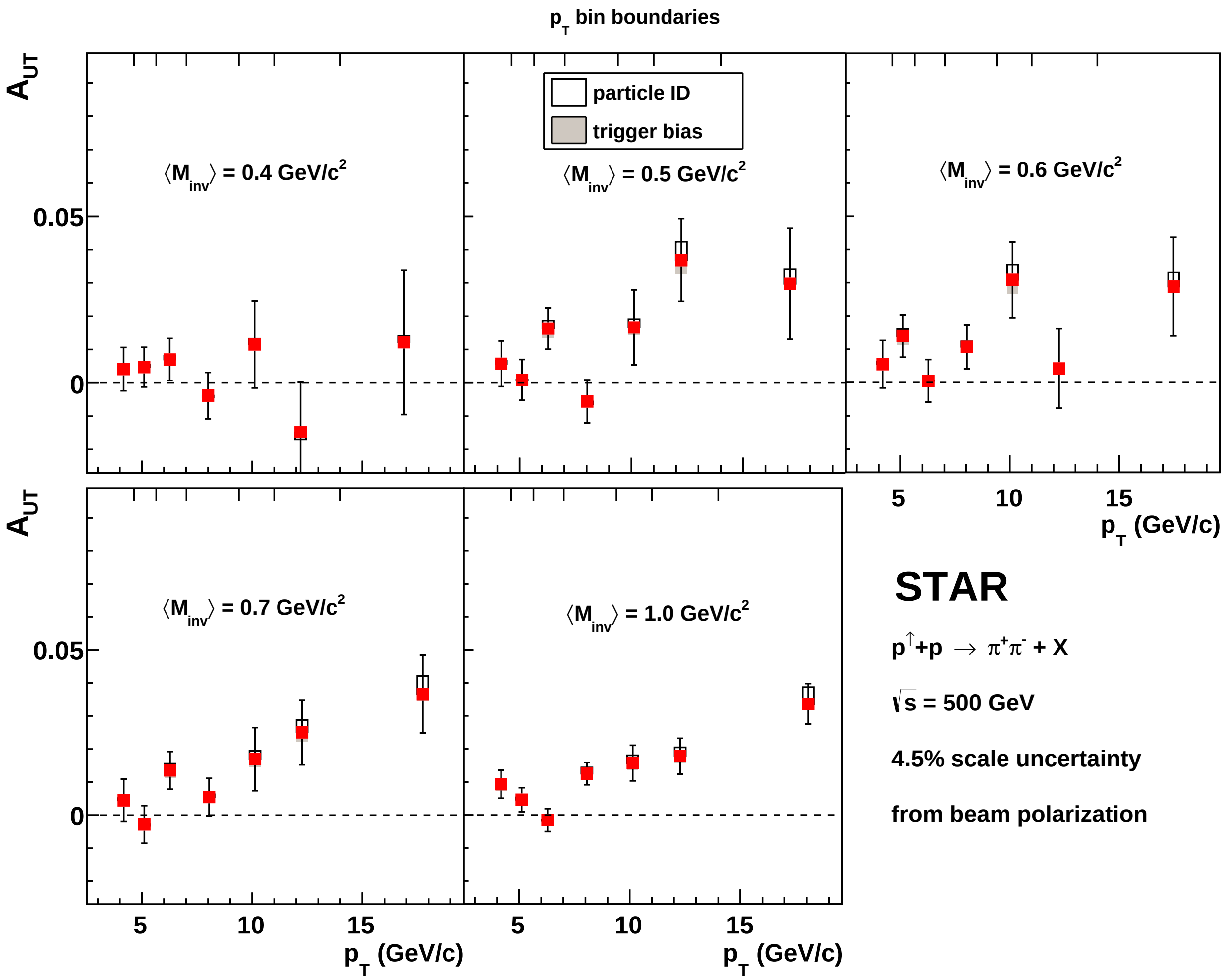

Fig. 5.6. The asymmetry A_{UT} as a function of $p_T^{\pi^+\pi^-}$ for all $M_{\pi^+\pi^-}$ bins and $\eta^{\pi^+\pi^-} > 0$.

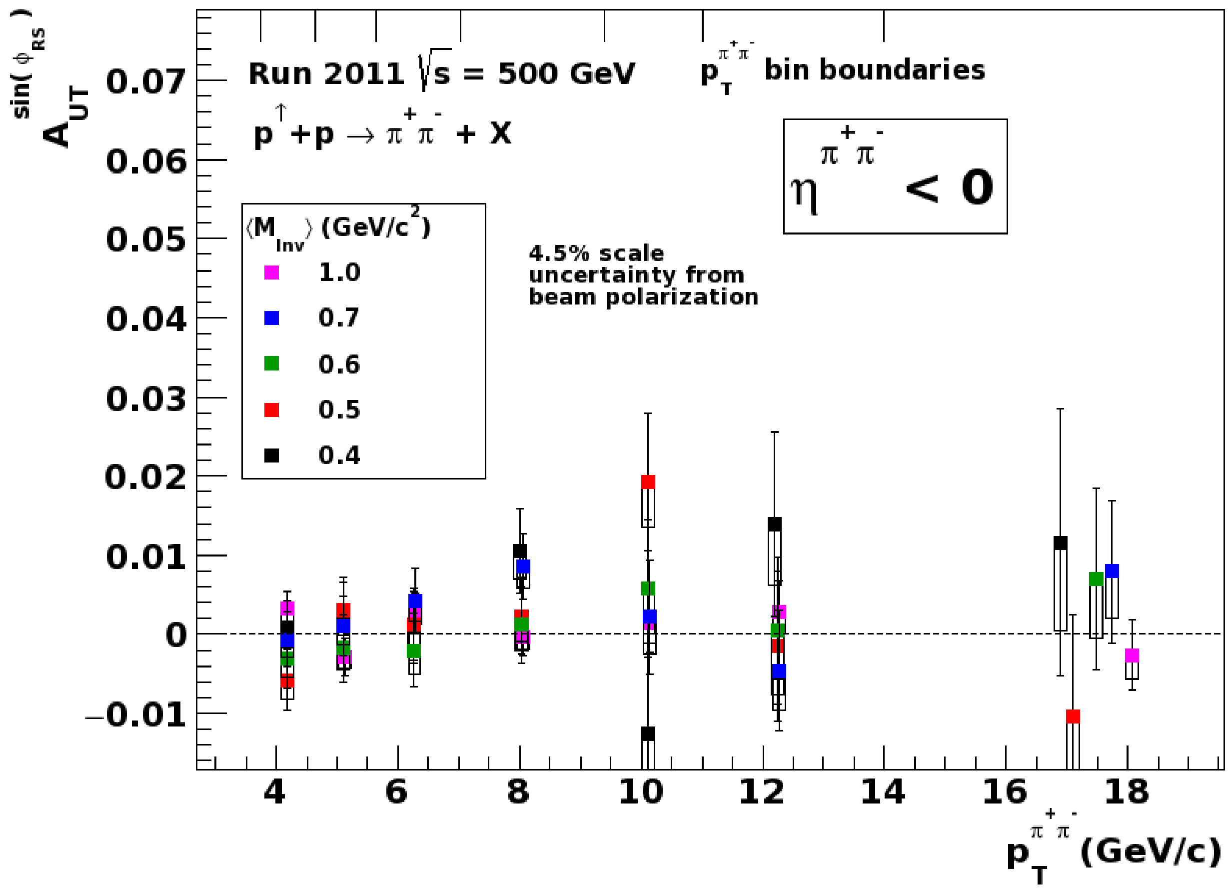

Fig. 5.7. The asymmetry A_{UT} as a function of $p_T^{\pi^+\pi^-}$ for all $M_{\pi^+\pi^-}$ bins and $\eta^{\pi^+\pi^-} < 0$.

ratio of a biased sample over the quark/gluon ratio in a unbiased sample as shown in Fig. 4.12.

Figure 5.8 shows the x range probed by measurements presented here(left panel) and where this range appears(shaded blue) with respect to previous measurements [10](right panel). x was determined from the aforementioned simulation. Compared to previous measurements STAR has measured asymmetries with high precision at relatively high x and a much higher effective Q^2.

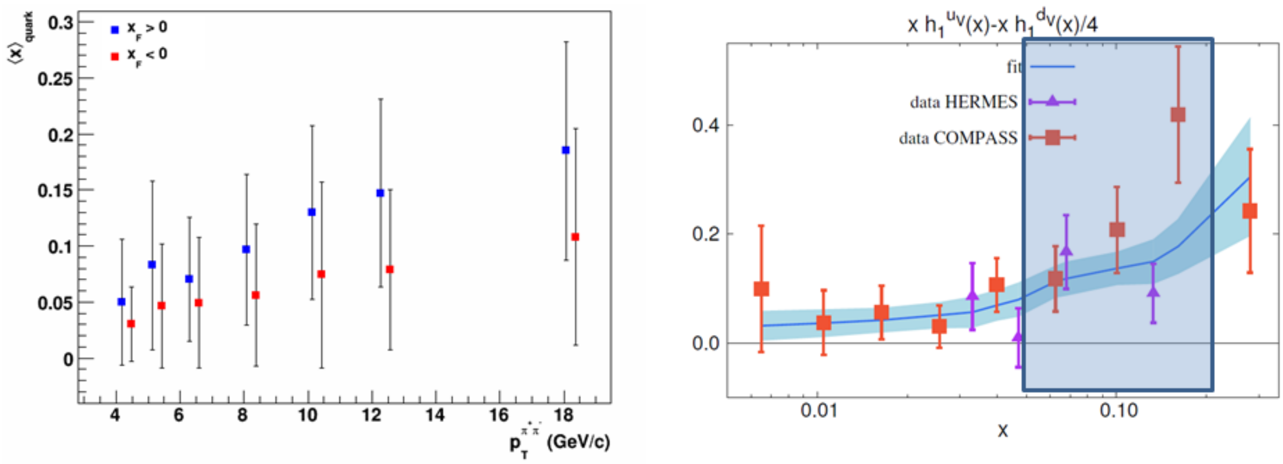

Fig. 5.8. (left)The average x of quarks in the forward(blue) and backward(red) direction as a function of $p_T^{\pi^+\pi^-}$. Error bars represent the RMS of the x distribution. (right)The single spin asymmetry fit to HERMES and COMPASS data. The STAR x coverage is shaded blue.

6. SUMMARY

STAR has measured the first $\pi^+\pi^-$ correlation asymmetries in $p^\uparrow + p$ collisions at $\sqrt{s_{NN}} = 500$ GeV. Preliminary STAR data show high precision asymmetries at high $p_T^{\pi^+\pi^-}$ and $M_{\pi^+\pi^-}$ for $\eta^{\pi^+\pi^-} > 0$. These measurements are at much higher Q^2 and sample a different mixture of quark flavors than SIDIS. The results may be used to test universality of transverse polarization dependent quantities(SIDIS vs $p + p$).

LIST OF REFERENCES

LIST OF REFERENCES

[1] V. Barone, A. Drago, and P. G. Ratcliffe, *Phys. Rep.* **359**, 1 (2002).

[2] A. Vossen, *AIP Conf. Proc.* **1560**, 519 (2013).

[3] HERMES Collab. (A. Airapetian *et al.*), *Phys. Ret. Lett.* **94**, 012002 (2005).

[4] HERMES Collab. (A. Airapetian *et al.*), *JHEP* **0806**, 017 (2008).

[5] COMPASS Collab. (C. Adolph *et al.*), *Phys. Lett.* **B713**, 10 (2012).

[6] COMPASS Collab. (M. Alekseev *et al.*), *Phys. Lett.* **B692**, 240 (2010).

[7] COMPASS Collab. (M. Alekseev *et al.*), *Phys. Lett.* **B673**, 127 (2009).

[8] R. L. Jaffe, X. Jin, and J. Tang, *Phys. Rev. Lett.* **80**, 1166 (1998).

[9] D. Boer, R. Jakob, and M. Radici *Phys. Rev.* **D67**, 094003 (2003).

[10] A. Bacchetta, A. Courtoy and M. Radici, *JHEP* **1303**, 119 (2013).

[11] STAR Collab. (K. Ackermann *et al.*), *Nucl. Instrum. Methods* **A499**, 624 (2003).

[12] A. Bacchetta and M. Radici, *Phys. Rev.* **D70**, 094032 (2004).

[13] G. G. Ohlsen and P. W. Keaton, *Nucl. Instrum. Meth.* **109** (1973).

[14] T. Sjostrand, S. Mrenna, and P. Z. Skands, *JHEP* **0605**, 026 (2006).

[15] R. Brun *et al*, User guide and reference manual (1978).

LIST OF TABLES

LIST OF FIGURES